



## Design and characterization of MEMS micromotor supported on low friction liquid bearing

Mei Lin Chan<sup>a</sup>, Brian Yoxall<sup>a</sup>, Hyunkyu Park<sup>a</sup>, Zhaoyi Kang<sup>b</sup>, Igor Izyumin<sup>b</sup>, Jeffrey Chou<sup>b</sup>, Mischa M. Megens<sup>b</sup>, Ming C. Wu<sup>b</sup>, Bernhard E. Boser<sup>b</sup>, David A. Horsley<sup>a,\*</sup>

<sup>a</sup> Department of Mechanical and Aerospace Engineering, University of California at Davis, Davis, CA 95616, USA

<sup>b</sup> Department of Electrical Engineering and Computer Science, University of California, Berkeley, CA, USA

### ARTICLE INFO

#### Article history:

Received 16 April 2011

Received in revised form 3 August 2011

Accepted 4 August 2011

Available online 25 August 2011

#### Keywords:

Micromotor  
Liquid bearing  
Micromachining  
Hydrophobic  
Torque  
Magnetic drive

### ABSTRACT

This paper examines the performance of rotating microdevices incorporating a liquid bearing to couple a rotating element to a fixed substrate. Liquid bearing technology promises to significantly improve the durability and lifetime of micromechanical motors. Here, the fluid is confined between the rotor and stator using surface patterning of a hydrophobic layer. Magnetic actuation of 10 mm diameter silicon rotor is used to characterize the liquid bearing motor at rotation rates up to 1800 rpm. Bearings with fluid thickness from 20 to 200  $\mu\text{m}$  are characterized. A minimum torque of 0.15  $\mu\text{N}\cdot\text{m}$  is required to initiate rotation. At rotation rates above 720 rpm, the rotor wobble is less than  $\pm 1$  mrad and the bearing exhibits viscous friction with a drag coefficient of  $1.2 \times 10^{-3}$   $\mu\text{N}\cdot\text{m}/\text{rpm}$ . The drag performance of the disk-type liquid bearing using  $\text{H}_2\text{O}$  as the fluid is approximately 15 times lower than that demonstrated in a micro-ball bearing supported rotor.

© 2011 Elsevier B.V. All rights reserved.

### 1. Introduction

Surface tension and friction are dominant forces at small length scales. In this expanded effort based on the previous work [1], we exploit surface tension to overcome friction limitations in rotating microdevices by supporting a freely-rotating payload on a liquid rotary bearing. There are many instances of MEMS rotary motors in the literature. Examples include center-pinned wobble motors that have been actuated electrostatically [2,3], ultrasonically [4] and magnetically [5] as well as motors incorporating micro-ball bearings [6]. A systemic problem with solid–solid contacts between the rotating parts and frame elements is friction. To minimize the effect of friction and wear in macroscale devices, fluid lubricating layers are often used to remove direct solid–solid contact. These lubricating layers take the form of externally pressurized gas-lubricated hydro-dynamic bearings [7] and “air” bearings created through electrostatic or magnetic suspension [8,9]. These support mechanisms often require complex manufacturing processes with tight fabrication tolerances and complicated control schemes.

Here, instead of using pressurized fluid to provide the thrust for bearing support, surface tension between a thin liquid film and the patterned rotor and stator surfaces acts as the support mechanism. Although the liquid bearing principle has been demonstrated [10,11] using electrowetting as the driving mechanism, little quantitative performance data or analytical modeling have been presented to date. As demonstrated herein, liquid bearing technology is wear-resistant, capable of supporting both static and dynamic loads, and is self-centering.

In this work, the focus is on the design and characterization of the liquid bearing structure. The bearing technology can be used with various actuation methods but magnetic actuation was chosen here over electrostatic actuation due its simpler fabrication and lack of pull-in instability. Using methods similar to earlier magnetic micromotors [5,12], permanent magnets are assembled onto the silicon rotor and external coils are used to generate magnetic flux, allowing rotation rates over 1800 rpm. We present experimental data on the load-bearing capacity, viscous drag characteristics and wobble of the liquid bearing micromotor using water and ethylene glycol (EG) as the liquid layer in three different bearing geometries (disk, ring and full coverage). Static and dynamic loading characteristics of the liquid bearing motor are also determined. A self-centering characteristic observed in one of the bearing designs is analyzed and liquid bearing packaging and lifetime issues are addressed.

\* Corresponding author at: Department of Mechanical and Aerospace Engineering, One Shields Avenue, Bainer Hall, Davis, CA 95616, USA. Tel.: +1 530 752 1778; fax: +1 530 752 4158.

E-mail address: [dahorsley@ucdavis.edu](mailto:dahorsley@ucdavis.edu) (D.A. Horsley).

## 2. Operating principle

Fig. 1 shows a schematic drawing of the liquid bearing rotor and the experimental set-up used to magnetically actuate the liquid bearing motor. The bearing geometry is defined by patterning the surfaces of the rotor and stator with a 2  $\mu\text{m}$  thick hydrophobic amorphous fluorocarbon layer (Cytop, Asahi Glass Co.). The contact angles of water and EG on the Cytop surface are  $\sim 99$  and  $\sim 94$  degrees, respectively. The relatively high surface energy of glass and silicon allows the bearing liquid to wet the exposed surfaces, while the hydrophobic Cytop layer pins the bearing edges to a fixed location, as illustrated in Fig. 2a.

Surface tension effects provide centering and load carrying capability. The bearing thickness,  $h$ , investigated in this work lies in the range between 20 and 200  $\mu\text{m}$  thick, much smaller than the capillary length,  $l_c$ , of the liquids ( $l_{c,\text{H}_2\text{O}} = 2.7$  mm,  $l_{c,\text{EG}} = 2$  mm) in order to ensure that surface tension dominates over gravitational force on the fluid.

In response to a transverse force applied to the right edge of the rotor (see Fig. 2b), the contact angle of the liquid bearing changes and the restoring force due to surface tension is:

$$F_{\text{res}} = \sqrt{2}R\gamma_{LV}(\theta_R - \theta_L) \quad (1)$$

where  $\gamma_{LV}$  is the fluid surface tension ( $\gamma_{LV,\text{H}_2\text{O}} = 72.8$  mJ/m<sup>2</sup>,  $\gamma_{LV,\text{EG}} = 47.7$  mJ/m<sup>2</sup>),  $\theta$  is the contact angle and the subscripts  $R$  and  $L$  denote the contact angle at the right and left edges of the rotor and  $R$  is the bearing radius. For the bearing geometry under test, and assuming a contact angle offset ( $\theta_L - \theta_R$ ) =  $10^\circ$ , the restoring force,  $F_{\text{res}} \approx 100$   $\mu\text{N}$ , allowing the bearing to support a maximum transverse load equal to approximately 10% of the rotor's weight. The rotor mass scales as  $R^2$  while the transverse retention force scales as  $R$ , so the bearing's ability to support transverse forces improves dramatically as the motor radius decreases, and suggesting that a motor with a 1 mm diameter rotor could operate in a vertical orientation.

For motion in a direction normal to the rotor face, as illustrated in Fig. 2c and d, a lifting force,  $F_{\text{sup}}$ , or an adhesion force,  $F_{\text{pulloff}}$ , results from both Laplace pressure and surface tension:

$$F_{\text{normal}} = \frac{2\pi R^2 \gamma_{LV}}{h} \cos \theta + 2\pi R \gamma_{LV} \sin \theta \quad (2)$$

where  $h$  is the bearing thickness. The contact angle between the liquid bearing and the surface,  $\theta$  is assumed to be the same at all edges of the disk and is critical in determining the forces acting on the rotor.

A liquid bearing with low viscosity,  $\mu$  ( $\mu_{\text{H}_2\text{O}} = 1$  mPa s,  $\mu_{\text{EG}} = 16.1$  mPa s), allows the rotor to operate in a low friction domain. The viscous friction characteristics of the liquid bearing are a function of fluid thickness and radius and are modeled by the viscous drag coefficient,  $b$ :

$$b = \frac{\mu\pi R^4}{2h} \quad (3)$$

Static friction properties of the bearing have a more complicated origin, depending on both the curvature of the bearing edge and roughness created by imperfections of the bearing boundary.

## 3. Design and fabrication

The fabrication process for both rotor and stator is detailed in Fig. 3. The stator is fabricated from a 700  $\mu\text{m}$  thick glass substrate while the rotor is 10 mm diameter disk made from a 300  $\mu\text{m}$  thick silicon wafer. Fig. 3j–m shows the stator layer fabrication procedure in which a photoresist liftoff process is used to pattern the Cytop film that defines the shape and size of the liquid bearing. A 3  $\mu\text{m}$  thick positive photoresist (Megaposit SPR220-3, Rohm and Haas) is

spin-coated and patterned by photolithography to define the circular confinement region for the liquid bearing. The Cytop thin film is then spin-coated at 1500 rpm onto the wafers. After hard baking at  $110^\circ\text{C}$  for 10 min, unnecessary Cytop and photoresist patterns are stripped in acetone, then rinsed in methanol and D.I. water.

The rotor fabrication begins with a double side polished 4-in. silicon wafer. A Cytop layer is first defined on the bottom surface of the wafer using liftoff as described above. On the top side of the wafer, a trench is etched using deep reactive ion etching (DRIE) to 80  $\mu\text{m}$  depth to define the housing for the magnet. To ensure concentricity of the bearing pattern on the rotor, the rotor's cylindrical shape is lithographically aligned to the bearing pattern on the backside of the wafer using 10  $\mu\text{m}$  thick photoresist (KMPR 1005, MicroChem) and DRIE is used to etch through the 300  $\mu\text{m}$  thick wafer.

A 1.5 mm NdFeB magnet cube with magnetic moment,  $m$ , of  $4.1 \times 10^{-3}$  A m<sup>2</sup> is centered and mounted on top of the rotor. The mass moment of inertia of the rotor is  $6.96 \times 10^{-10}$  kg m<sup>2</sup> and  $6.86 \times 10^{-10}$  kg m<sup>2</sup> with and without the magnet, respectively; while the total weight of the rotor-magnet structure is  $\sim 90$  mg. Fig. 4 shows side and bottom views of a complete (stator/liquid-bearing/rotor) device assembled using a vacuum pick-and-place technique. In Fig. 4a, the side view of the assembled rotor shows the liquid bearing colored with a red dye to help visualize position. The bottom view is taken through the glass stator focusing on the liquid bearing and the bottom of the rotor. This view highlights the single-droplet liquid bearing structure with 10  $\mu\text{l}$  of liquid confined within the 6 mm diameter annular patterned Cytop layer. The outer ring of electrodes on the rotor was designed for electrostatic driving but was not employed in this work.

The mechanical performance of the liquid bearing micromotor was characterized using magnetic actuation to spin the rotor. Two orthogonal pairs of Helmholtz coils are driven with currents that are  $90^\circ$  out of phase, at matched amplitudes, to create a rotating magnetic field with uniform magnitude in the range of  $B = 1$  mT. The frequency of the coil signal,  $\Omega$ , determines the motor rotation rate while the field amplitude provides control over the applied torque.

## 4. Performance

### 4.1. Static pull-off force measurements

As described by Eq. (2), surface tension creates either adhesive or repulsive forces to: (1) prevent separation of rotor from stator or (2) support the rotor. In the case where the motor is inverted and gravity pulls the rotor away from the stator, as illustrated in Fig. 2d, a concave-shaped meniscus bridge forms between the hydrophilic part of the stator and rotor. Referring to Eq. (2), the concave shape of the liquid interface ( $\theta < 90^\circ$ ) results in negative Laplace pressure inside the bearing liquid. This negative pressure results in an intrinsic adhesive force between the stator and rotor and retains the rotor in place. On the other hand, when the motor is upright, the gravitational force compresses the bearing and the liquid interface assumes a convex shape. A convex meniscus interface angle ( $\theta > 90^\circ$ ) creates a positive Laplace pressure and repulsive  $F_{\text{sup}}$ , as illustrated in Fig. 2c. The contact angle between the fluid and Cytop surface defines  $\theta_{\text{max}}$  and thus  $F_{\text{sup,max}}$  for the bearing.

A quasi-static loading measurement using an electronic microbalance (A&D HR2021) with a sensitivity of 0.01 mg was conducted to determine both the tensile pull off force required to separate the rotor from the liquid surface and the compressive load carrying capability of the rotor. The assembled micromotor of the disk bearing design was placed inside the microbalance. Care was taken to run the experiment in a saturated vapor pressure environment by placing a beaker of supersaturated salt solution in

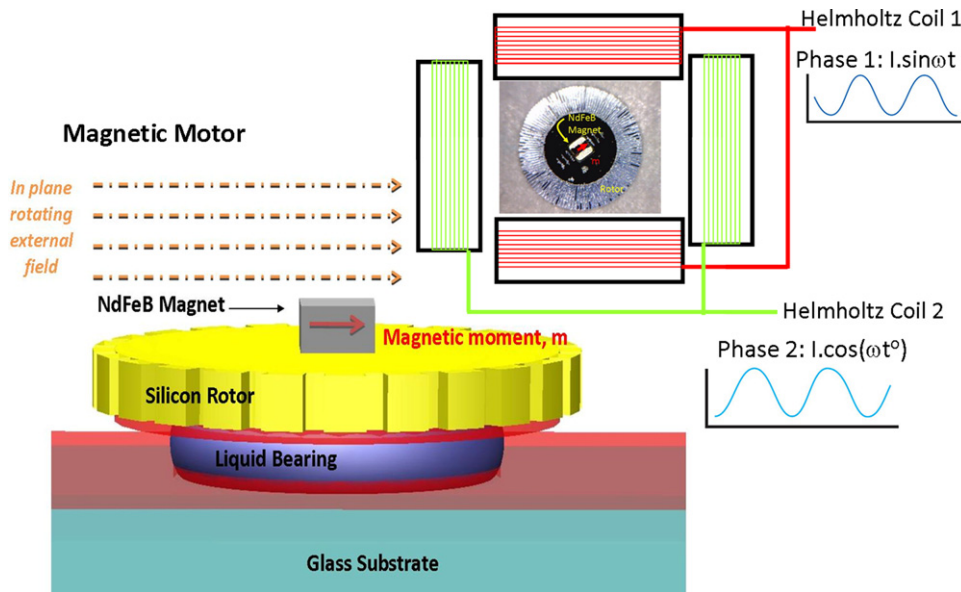


**Fig. 1.** Schematic of the liquid bearing structure used to support a silicon rotor on a glass substrate. An NdFeB magnet mounted on the silicon rotor follows the rotating magnetic field generated by the two-axis Helmholtz coils.

the measuring chamber. The breeze break doors of the microbalance were closed or shielded to remove any air currents, and the experiments were run immediately after assembly to minimize any changes in liquid bearing volume due to evaporation. The rotor was attached to one end of a freely suspended string, while the other end was attached to a motorized linear actuator, (M230, Physik Instrumente) with a minimum step motion of 50 nm. Using a servo controller (C863 Mercury, Physik Instrumente), the rotor was lifted at a speed of 0.001 mm/s in a number of steps until the liquid bearing meniscus broke apart and the rotor was detached. At each translation step, the mass readout of the electronic balance was recorded after allowing the readout to stabilize. The retention force exerted by the liquid on the rotor is plotted against the relative displacement of the linear actuator in Fig. 5a for liquid bearings with various volumes of ethylene glycol (EG).

Initially, the force readout remains unchanged as the actuator translates upwards, corresponding to tensioning of the string, as indicated by the inset figures. When the string is in tension, the tensile load is transferred to the bearing and deformation of the liquid bearing meniscus occurs as shown in Fig. 5b. The liquid bridge

gradually necks (Fig. 5c) and eventually breaks off (Fig. 5d) as shown in the sudden change in force, indicating rotor pull off. The minimum of each curve indicates the maximum tensile load that the rotor can sustain which is highly dependent on the thickness of the bearing. For a bearing with 85 μm thickness, the pull off force is determined to be ~12.9 mN.

In the small displacement regime, the experimental results agree with the analytical model described in Eq. (2) within a factor of 2, a reasonable result given uncertainty about the initial bearing thickness and static contact angle. However, in the necking regime, the assumptions underlying the analytical model that the radii of the solid–liquid contact lines are very small compared to both the bearing radius,  $R$  and bearing height,  $h$  no longer holds true.

#### 4.2. Dynamic loading measurements

To qualitatively examine the behavior of the bearing under dynamic loading, the rotor and bearing were assembled on a stator patterned at the end of a glass slide. The other end of the glass slide was mounted onto a clamp and an impulse hammer was used to

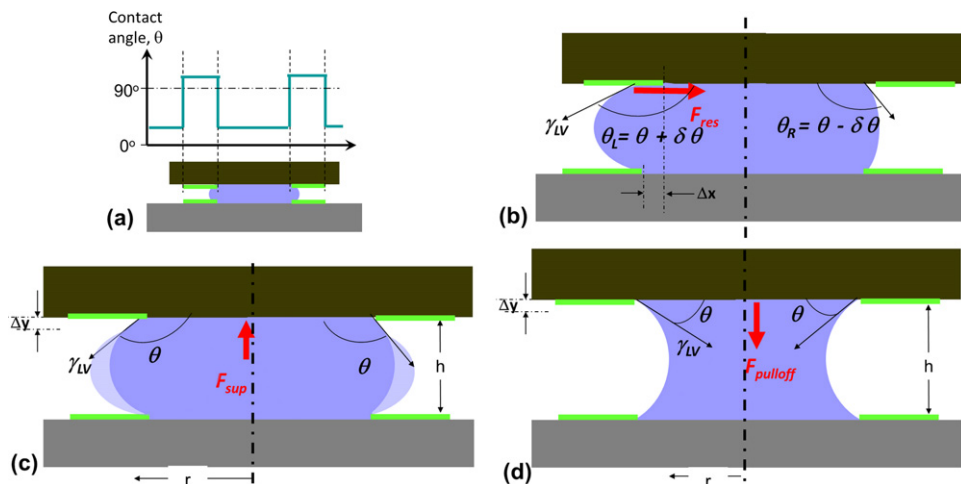


**Fig. 2.** (a) Schematic of the cross section of the liquid bearing structure with variations in contact angle from non-wetting to wetting regions, forces acting on the rotor due to surface tension to (b) center the rotor (c, d) support the rotor in compression and tension.

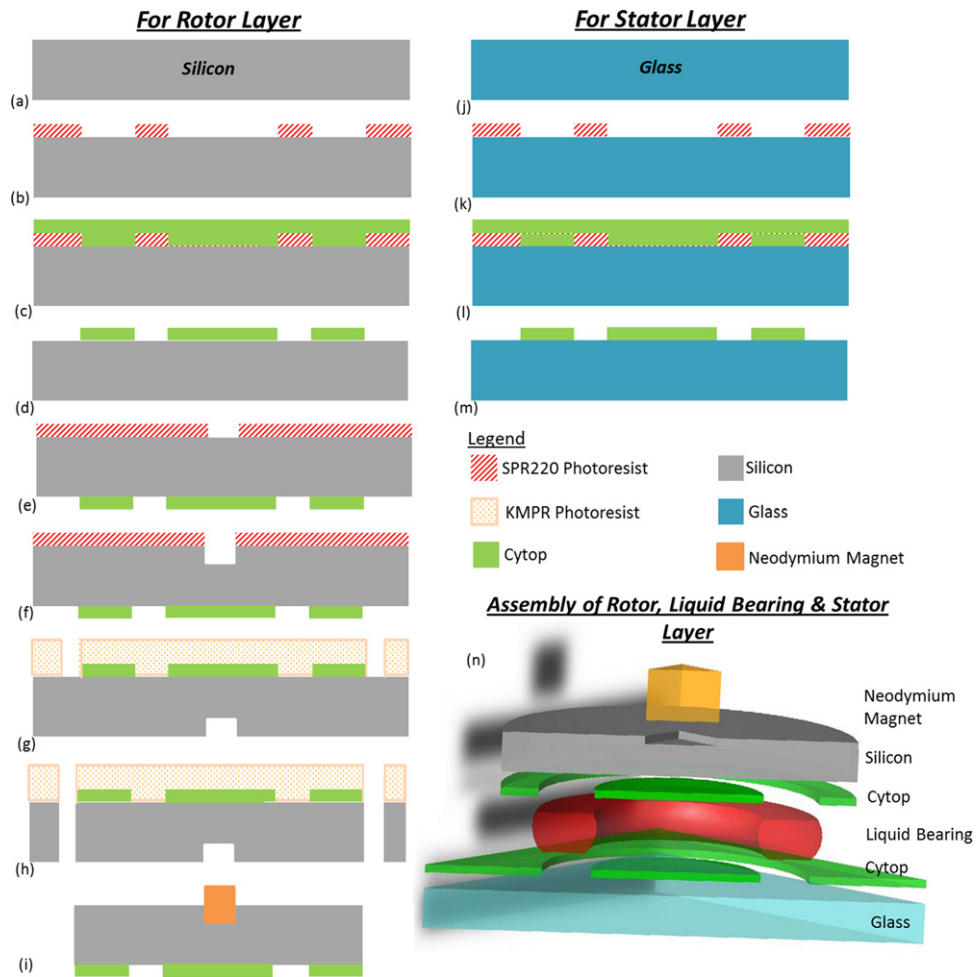


**Fig. 3.** Schematic of the microfabrication process for both Si rotor (a–i) and glass stator (j–m), (n) cross-section exploded view of a complete (stator/liquid-bearing/rotor) device.

excite the slide at the fixed end. The resulting acceleration of the rotor was computed by differentiating the velocity measured using a Laser Doppler Vibrometer, LDV (Polytec). The results of experiments conducted with motor mounted in both the upright and inverted formats are shown in Fig. 6a and b, respectively.

The rotor and bearing survived a test with base input acceleration equal to  $\sim 60 g$  and  $\sim 15 g$  in the upright and inverted configuration respectively, where  $g$  denotes the gravitational acceleration =  $9.81 \text{ m/s}^2$ . However, these data points do not indicate the

point of catastrophic failure, where the rotor detaches away from the stator, but the limitations of the experimental set-up.

4.3. Torque measurements

The rotation characteristics of three different geometries of the liquid bearing, shown in Table 1, were investigated. For both the ring and disk bearings, the shape of the bearings is confined by the patterned Cytop layer. In the case of the full bearing design,

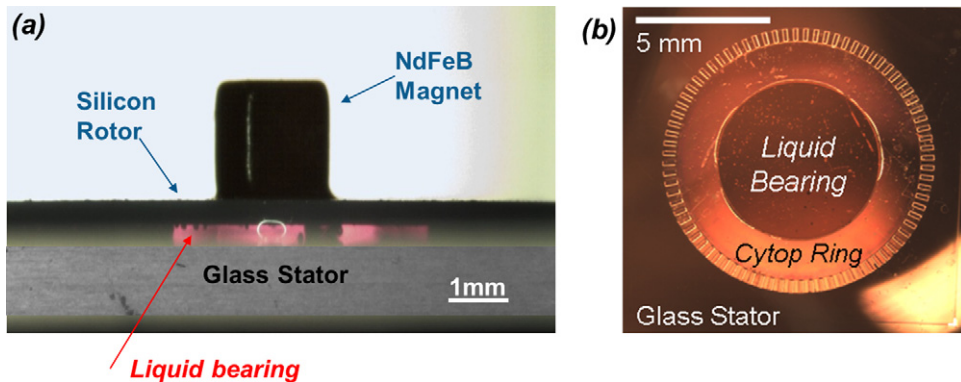


**Fig. 4.** (a) Side view of the rotor sitting on a liquid bearing and (b) optical micrograph through the glass stator showing the confinement of the liquid within the patterned Cytop ring. The diameter of the liquid bearing is 6 mm.

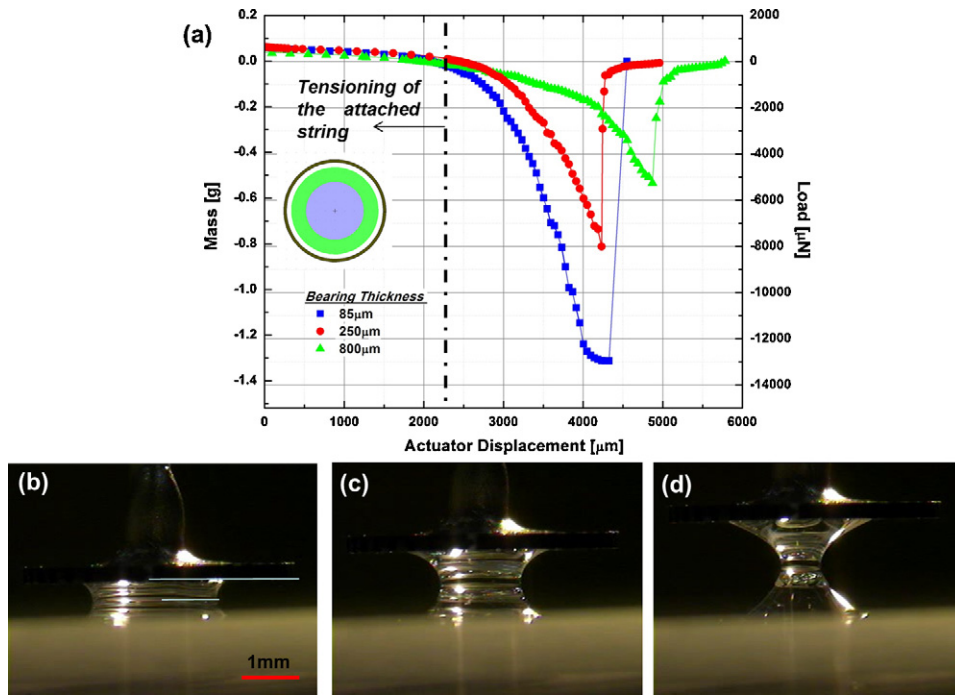


**Fig. 5.** (a) Static loading characteristics of the liquid bearing, series of optical images taken as the liquid bearing is (b) loaded (c) deformed and (d) undergoing necking before breaking off.

the liquid is trapped under the rotor and within a 300 μm wide circumferential gap around the rotor periphery.

The drag induced by the liquid bearing during rotation is an important performance metric that has not been measured in prior work. The total drag of the bearing,  $\tau_b$ , is speed dependent and the bearing exhibits both viscous and static friction (stiction). The magnetic torque applied to the rotor,  $\tau_{applied}$ , is a function of the phase

angle,  $\phi$ , between the external field,  $B$ , and the magnetic moment of the permanent magnet,  $m$ ,

$$\tau_{applied} = \vec{m} \times \vec{B} = |m| |B| \sin \phi \quad (4)$$

Since all the parameters of Eq. (3) are known or can be measured, the drag torque of the liquid bearing can be measured, as demonstrated below.

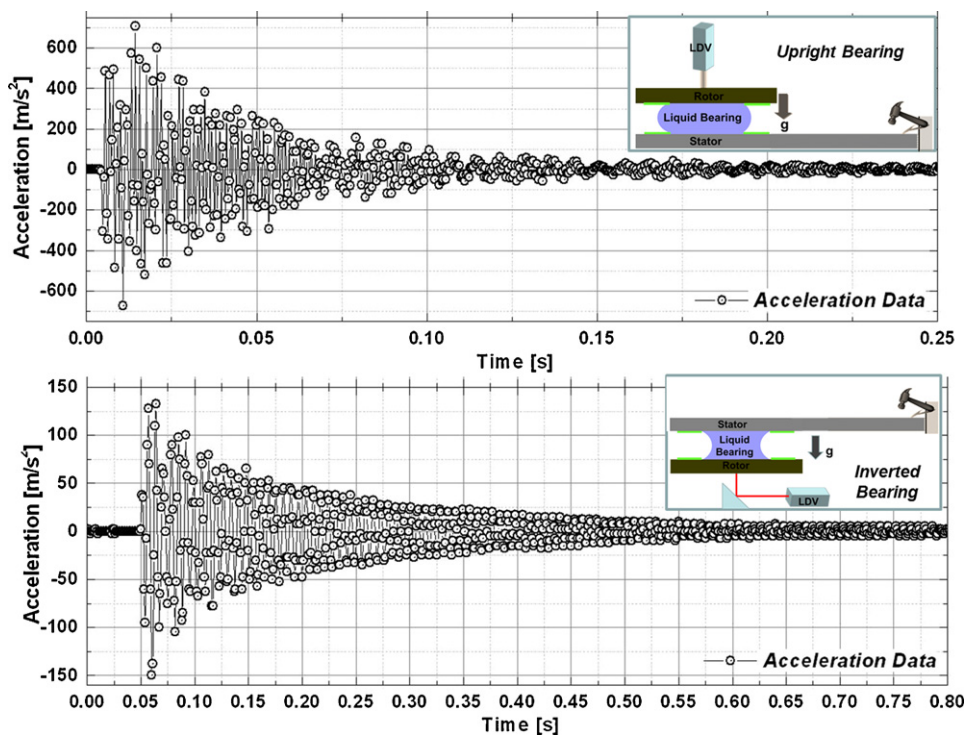


**Fig. 6.** Time response of the liquid bearing supported rotor under a random base excitation for (a) upright and (b) inverted configurations. Figure inset illustrates the test configuration.

**Table 1**  
Table of the varying liquid bearing geometries used in the measurements.

Bearing Design	Disk Bearing	Ring Bearing	Full Bearing
Top View of Bearing			
Cross Section View of Bearing			
Rotor Radius [mm]	5	5	5
Bearing Radius [mm]	3	Inner = 1.5, Outer = 3.5	5

#### 4.3.1. Start-up torque requirement

Startup torque,  $\tau_s$ , is defined as the minimum  $\tau_{applied}$  for the rotor to begin spinning. Fig. 7 shows experimental measurement of  $\tau_s$  for different bearings geometries, fluid thicknesses and viscosities. The data show an exponential dependence on the fluid bearing thickness,  $h$ . Moreover, the startup torque for the EG bearing is only slightly larger than that for H<sub>2</sub>O, indicating that that fluid viscosity does not play an important role at slow rotation rates.

In the case of both ring and disk bearings, the bearing becomes less stable in tip/tilt as the thickness of the bearing increases. The edges of the tipping rotor contact the stator, resulting additional stiction and an increased startup torque. This tip/tilt instability is not apparent in the full coverage bearing, allowing the fluid bearing to operate with a thicker fluid layer. The start-up torque for the full bearing remains constant at 0.15  $\mu\text{N}\cdot\text{m}$  for fluid thickness  $h > 120 \mu\text{m}$ .

#### 4.3.2. Viscous friction drag

For fluid bearings thicker than 100  $\mu\text{m}$ , startup torque is small and bearing drag torque, is dominated by viscous drag torque,  $\tau_v = b\Omega$ , where  $\Omega$  is the rotation rate and  $b$  is the viscous drag coefficient (defined in Eq. (3) above). When the friction is less than  $\tau_{max} = \max(\tau_{applied}) = |m||B|$ , increasing  $\Omega$  increases drag and the

phase angle,  $\phi$ , approaches 90°. The critical rate of rotation occurs when  $\tau_v = \tau_{max}$ , above which the rotor oscillates at the excitation frequency but does not spin. Fig. 8 shows that the maximum rotation rate depends linearly on both the liquid bearing thickness and the applied torque, consistent with the viscous friction model.

The mean viscous drag coefficient calculated experimentally as  $b = |m||B|/\Omega_{max}$  for disk bearing designs from 110 to 150  $\mu\text{m}$  thick, is  $1.2 \times 10^{-3} \mu\text{N}\cdot\text{m}/\text{rpm}$  which is 20% higher than Eq. (4) predicts using known values for the fluid viscosities. This result can be attributed to measurement uncertainty in the bearing thickness during torque measurements. The friction coefficient of the disk-type liquid bearing using H<sub>2</sub>O as the fluid is approximately 15 times lower than that demonstrated in a micro-ball bearing supported rotor [6]. For an input torque of 1.6  $\mu\text{N}\cdot\text{m}$ , the maximum rotation rate as a function of the bearing thickness is calculated to be 0.225 rps/ $\mu\text{m}$  for the disk shaped H<sub>2</sub>O bearing.

#### 4.3.3. Maximum rotation rate

In Fig. 8, for liquid bearings at  $\sim 145\text{--}150 \mu\text{m}$  thickness, with a  $\tau_{applied}$  of 1.60  $\mu\text{N}\cdot\text{m}$ , the maximum rotation rate achieved was  $\Omega_{max} = 30 \text{ Hz}$ , or 1800 rpm. Fig. 9 shows images of the rotor at rest, during spin up and at a constant rate of rotation of 1800 rpm. The

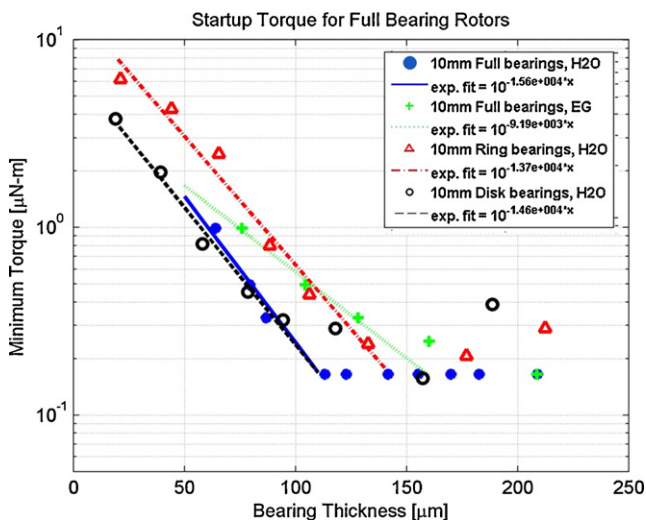


**Fig. 7.** Experimental data showing the trend of the startup torque with respect to varying bearing thickness and bearing geometries.

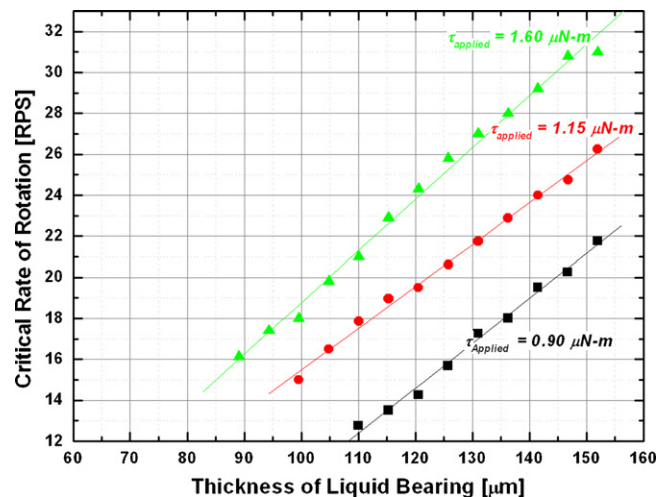


**Fig. 8.** Experimental data showing the maximum rotation rate above which the rotor fails to follow the magnetic field. Measurements were conducted over different bearing thicknesses and magnetic torque levels to identify the parameters of the viscous friction model.

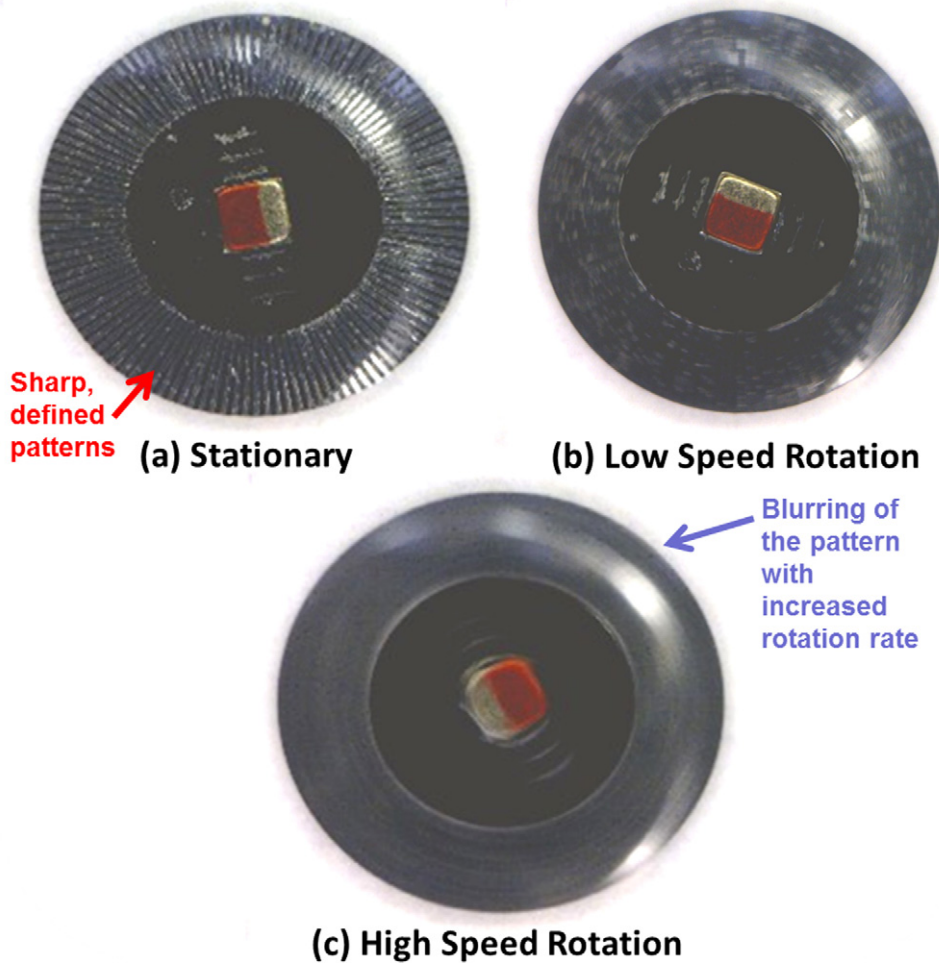


**Fig. 9.** Three video capture frames showing the magnetically actuated motor (a) at rest, (b) undergoing low speed rotation, and (c) rotating at a maximum rotation rate of 1800 rpm. When the motor is stationary, the etched markings at the circumference of the rotor are well defined. As the motor spins at higher speed, the rotational motion causes the markings to blur.

rotors can be actuated in the upright mode as well as the inverted mode.

#### 4.4. Wobble

Wobble is a measurement of the angular displacement of the rotor's normal axis relative to the stator's normal axis. Various effects contribute to wobble on a spinning liquid bearing rotor: (1) eccentricity error due to misalignment of the bearing with respect to rotor, (2) cogging due to surface defects at the edge of the bearing, (3) imbalanced magnetic torque due to the fact that the magnet's center is not coplanar with the liquid bearing, and (4) center of mass offset due to alignment error of the magnet mounted on the rotor. This last effect, misalignment of the magnet to the rotor which manifests itself as significant static rotor tilt, was the dominant error source observed in experiments.

To measure wobble in our system, a laser beam is reflected off the rotor surface at  $\sim 45^\circ$  to the stator normal into a 2-axis position sensitive photodiode (PSD). The wobble trajectory of a full liquid bearing rotor spinning at speed of  $\sim 500$  rpm is plotted for several revolutions in Fig. 10. The recorded data shows both a large 1.3 mrad repetitive component (due to static tilt of the rotor) as well as a smaller 0.3 mrad non-repetitive component.

For both the ring and disk bearings, the wobble is significant at all speeds. However, in the case of the full bearing, the wobble is only significant at low speeds ( $<180$  rpm). As described below,

dynamic self-centering created at higher rotation rates by the circumferential fluid film helps to center the bearing and maintain a uniform gap between the rotor and stator, preventing contact and allowing smoother free rotation.

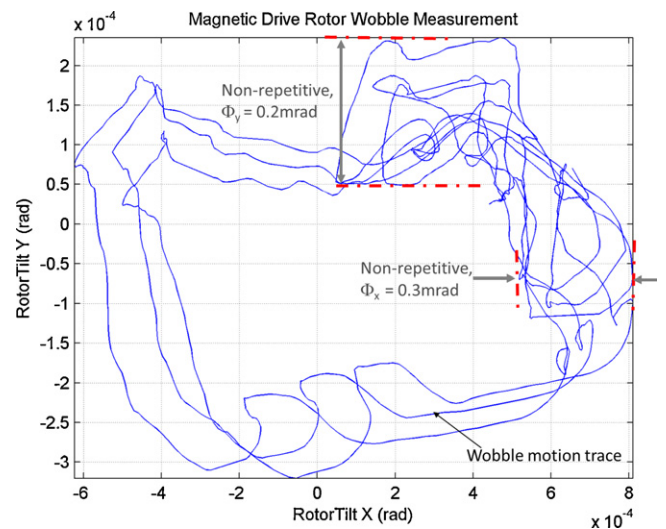


**Fig. 10.** Dynamic trajectory of the full bearing rotor spinning at a rotation rate of 500 rpm. The width of the full repetitive wobble trace is  $\sim 1.4$  mrad, while the non-repetitive component is shown to be  $\sim 0.3$  mrad.

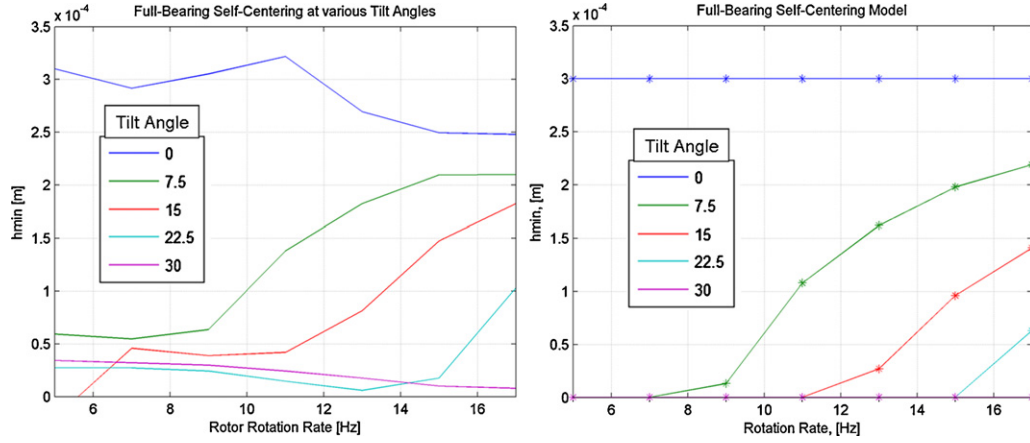


Fig. 11. (a) Measurement of eccentricity vs. rotation rate and liquid bearing tilt angle, and (b) model of eccentricity vs. rotation rate and liquid bearing tilt angle.

#### 4.5. Hydrodynamic self-centering effect

Noticeable self-centering of the full bearing supported rotor during start-up torque tests led to characterization of the centering effect. The rotational test bed was modified to operate with the rotor normal vector at various tilt angles,  $\phi$ , relative to gravity,  $G$ , providing a de-centering force on the rotor,  $F_{decenter}$ , as a function of the rotor mass,  $m$ :

$$F_{decenter} = mG \sin(\phi) \quad (5)$$

The self-centering is quantified using the eccentricity,  $e$ , which is the distance between the rotor and stator centers, and can vary between 0 and the clearance,  $C$ , which is the distance between rotor edge and stator wall when  $e=0$ . An alternative measurement is  $h_{min} = C - e$ , the minimum distance between rotor edge and stator for a given  $e$ . The normalized eccentricity is  $\varepsilon = e/C$  and is related to  $h_{min}$  by  $h_{min} = C(1 - \varepsilon)$ .

Fig. 11 shows measured eccentricity as a function of tilt angle and rotation rate. When the motor is level,  $\phi = 0$ , and self-centering is complete at all rotation rates,  $\Omega$ . However, when the motor is not level, the decentering force is non-zero and a threshold  $\Omega$  must be achieved before  $h_{min}$  rises above zero and the rotor separates from the stator wall.

Several models were investigated to explain the observed self-centering effect of the full-bearing configuration. The rotation rate dependence suggested an analogy to a journal bearing [13,14], where a fluid film between the rotor and stator walls builds up a pressure differential with rotational velocity, providing a force counter to  $F_{decenter}$  that separates the two bodies. Analytical and computational models of journal bearing performance under-predicted the observed centering effect by several orders of magnitude, predicting a separation  $h_{min}$  of only a fraction of a micrometer at rotation rates below 30 Hz. A second model was developed by accounting for energy loss from friction drag, and noting that the rotor would move to the position with the smallest energy loss.

The self-centering model which most closely matches the test data minimizes the total energy in the system, with kinetic energy calculated for the rotating liquid bearing and potential energy as a function of rotor eccentricity as shown in Eq. (6).

$$E_{total} = E_k + E_p = \sum_i \iiint_{r_i, \theta, z_i} \rho_{LB} r^2 \cdot r dr d\theta dz + ((\rho_{Si} - \rho_{LB}) \pi R_{rotor}^2 t + m_{magnet}) \cdot G \cdot e \sin(\phi) \quad (6)$$

where  $\rho_{LB}$  and  $\rho_{Si}$  are densities of the liquid bearing fluid and silicon, respectively,  $m_{magnet}$  is the mass of the magnet,  $r$ ,  $\theta$  and  $z$

are integration parameters (radial distance from rotor center, angle around rotor, and height above stator respectively) and the summation term  $i$  results from performing the integration over different regions of liquid bearing.

Fig. 12 shows energy calculations for various rotation rates as a function of eccentricity in a  $7.5^\circ$  tilt configuration, with marks on the curves at the minimum energy positions. The minimum energy positions from Fig. 12 are plotted as the  $7.5^\circ$  tilt line in simulated eccentricity data in Fig. 11b. Similar plots were created using the energy model for tilt angles from 0 to 30 degrees and good agreement is observed between the experimentally measured eccentricity, Fig. 11a, and the simulated eccentricity predicted using the energy model, Fig. 11b.

#### 4.6. Reliability

Selecting the right type of liquid as the bearing material is critical in determining the lifetime and reliability of these motors. Water has low viscosity and high surface tension but suffers from a high vapor pressure. In a laboratory environment, unpackaged water bearings were observed to last on the order of 10 min before evaporation rendered the micromotor useless. Ethylene glycol bearings were observed to last for more than 24 h but have higher viscosity

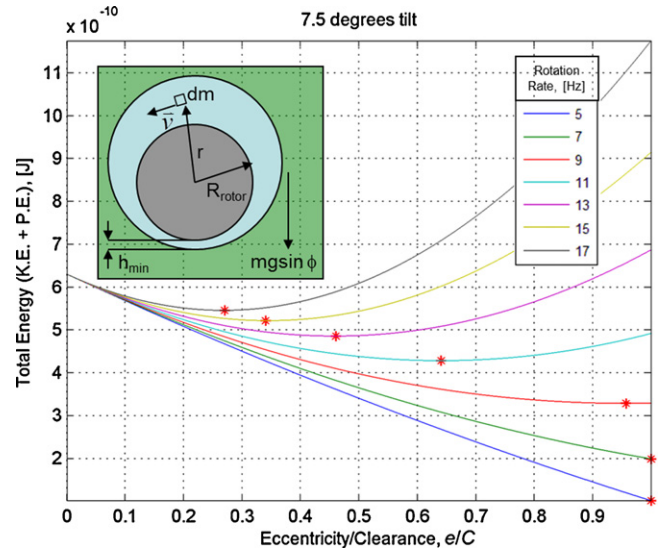


Fig. 12. Total energy (including kinetic energy and potential energy) of the rotor and liquid bearing system for rotation rates between 5 and 17 Hz rotation rate plotted vs. rotor eccentricity. The minimum energy positions are indicated on each curve.

and lower surface tension than water. To analyze the lifetime of the micromotor in a packaged environment, a Polydimethylsiloxane (PDMS) package with a cavity for the liquid bearing micromotor was formed using standard PDMS molding techniques. The glass stator substrate and the PDMS mold both underwent oxygen plasma to render the sealing faces hydrophilic. After assembling of the liquid bearing and rotor on the stator, the PDMS mold was then aligned and sealed onto the glass stator.

The packaged device's weight was monitored over time in a weighing balance and set to spin in the Helmholtz coils to determine the rate of rotation and changes in the critical frequency. The package environment helped to reduce the rate of evaporation and improved the lifetime of the water bearing motor to 4 days and the ethylene glycol bearings to more than 12 days. Since PDMS does not provide a vapor-tight seal, it is expected that even longer lifetime can be achieved with improved packaging.

## 5. Conclusion

We have demonstrated a novel liquid bearing and characterized several important physical parameters governing the performance of liquid bearing rotating microdevices. The minimum torque required to spin the rotor is  $\sim 0.15 \mu\text{N}\cdot\text{m}$ , and rotation rates up to 1800 rpm were demonstrated. The drag performance of the disk-type liquid bearing using  $\text{H}_2\text{O}$  as the fluid is approximately 15 times lower than that demonstrated in a micro-ball bearing supported rotor. Torque measurements conducted at speeds greater than 720 rpm were consistent with a viscous friction model, with the drag constant showing an inverse dependence on the fluid thickness. The start-up torque required to initiate rotation was also shown to diminish with increasing fluid thickness up to  $h \sim 120 \mu\text{m}$ . The physical mechanism that contributes to the start-up torque is not well-understood but is likely due to imperfections at the bearing edge that lead to surface-tension-related stiction.

## Acknowledgement

This work is supported by DARPA under grant 31P4Q-10-1-0002. The authors would like to thank the support of UC Davis Nanofabrication Center and fabrication help from Dr. Andre Guedes.

## Appendix A. Supplementary data

Supplementary data associated with this article can be found, in the online version, at doi:10.1016/j.sna.2011.08.003.

## References

- [1] M.L. Chan, B. Yoxall, H. Park, Z. Kang, I. Izyumin, J. Chou, M.M. Megens, M.C. Wu, B.E. Boser, D.A. Horsley, Low friction liquid bearing mems micromotor, in: IEEE 24th International Conference on Micro Electro Mechanical Systems (MEMS), 2011, pp. 1237–1240.
- [2] L.S. Fan, Y.C. Tai, R.S. Muller, IC-processed electrostatic micromotors, *Sensors and Actuators November* (20) (1989) 41–47.
- [3] M. Mehregany, S.F. Bart, L.S. Tavrow, J.H. Lang, S.D. Senturia, M.F. Schlecht, A study of three microfabricated variable capacitance motors, *Sensors and Actuators A: Physical February* (21) (1990) 173–179.
- [4] V. Kaajakari, A. Lal, Micromachined ultrasonic motor based on parametric polycrystalline silicon plate excitation, *Sensors and Actuators A: Physical June* (137) (2007) 120–128.
- [5] C.H. Ahn, Y.J. Kim, M.G. Allen, A planar variable reluctance magnetic micromotor with fully integrated stator and coils, *Journal of Microelectromechanical Systems December* (2) (1993) 165–173.
- [6] N. Ghahchehian, A. Modafe, M.I. Beyaz, R. Ghodssi, Design, fabrication, and characterization of a rotary micromotor supported on microball bearings, *Journal of Microelectromechanical Systems June* (17) (2008) 632–642.
- [7] L.G. Frechette, S.A. Jacobson, K.S. Breuer, F.F. Ehrich, R. Ghodssi, R. Khanna, C.W. Wong, X. Zhang, M.A. Schmidt, A.H. Epstein, High-speed microfabricated silicon turbomachinery and fluid film bearings, *Journal of Microelectromechanical Systems February* (14) (2005) 141–152.
- [8] S. Kumar, D. Cho, W.N. Carr, Experimental study of electric suspension for microbearings, *Journal of Microelectromechanical Systems March* (1) (1992) 23–30.
- [9] X.S. Wu, W.Y. Chen, X.L. Zhao, W.P. Zhang, Micromotor with electromagnetically levitated rotor using separated coils, *Electronics Letters August* (40) (2004) 996–997.
- [10] A. Takei, N. Binh-Khiem, E. Iwase, K. Matsumoto, I. Shimoyama, Liquid motor driven by electrowetting, in: Presented at the 2008 21st IEEE International Conference on Micro Electro Mechanical Systems – MEMS'08, Tucson, AZ, 2008.
- [11] A. Kajiwara, K. Suzuki, H. Miura, H. Takanobu, Study on micromotor using surface tension of liquid droplets, *Research Reports of Kogakuin University* (2006) 25–30 (October).
- [12] B. Wagner, M. Kreutzer, W. Benecke, Permanent magnet micromotors on silicon substrates, *Journal of Microelectromechanical Systems 2* (1993) 23–29.
- [13] M.M. Khonsari, E.R. Booser, *Journal Bearings*, John Wiley & Sons, Ltd., 2008.
- [14] E. Piekos, Numerical Simulation of Gas-lubricated Journal Bearings for Microfabricated Machines, Ph.D. Doctoral Thesis, MIT, Cambridge, MA, USA, 2000.